

Novel double channel reverse conducting GaN HEMT with an integrated MOS-channel diode

Xintong Xie(谢欣桐), Cheng Zhang(张成), Zhijia Zhao(赵智家), Jie Wei(魏杰),Xiaorong Luo(罗小蓉), and Bo Zhang(张波)

Citation: Chin. Phys. B, 2023, 32 (**9**): 098506. DOI: 10.1088/1674-1056/ace248
Journal homepage: http://cpb.iphy.ac.cn; http://iopscience.iop.org/cpb

What follows is a list of articles you may be interested in

Simulation design of normally-off AlGaN/GaN high-electron-mobility transistors with p-GaN Schottky hybrid gate

Yun-Long He(何云龙), Fang Zhang(张方), Kai Liu(刘凯), Yue-Hua Hong(洪悦华), Xue-Feng Zheng(郑雪峰),Chong Wang(王冲), Xiao-Hua Ma(马晓华), and Yue Hao(郝跃)
Chin. Phys. B, 2022, 31 (**6**): 068501. DOI: 10.1088/1674-1056/ac3739

Current oscillation in GaN-HEMTs with p-GaN islands buried layer for terahertz applications

Wen-Lu Yang(杨文璐), Lin-An Yang(杨林安), Fei-Xiang Shen(申飞翔), Hao Zou(邹浩), Yang Li(李杨), Xiao-Hua Ma(马晓华), and Yue Hao(郝跃)
Chin. Phys. B, 2022, 31 (**5**): 058505. DOI: 10.1088/1674-1056/ac2b1f

Performance analysis of GaN-based high-electron-mobility transistors with postpassivation plasma treatment

Xing-Ye Zhou(周幸叶), Xin Tan(谭鑫), Yuan-Jie Lv(吕元杰), Guo-Dong Gu(顾国栋), Zhi-Rong Zhang(张志荣), Yan-Min Guo(郭艳敏), Zhi-Hong Feng(冯志红), and Shu-Jun Cai(蔡树军)
Chin. Phys. B, 2021, 30 (**2**): 028502. DOI: 10.1088/1674-1056/abb7f6

Impact of oxygen in electrical properties and hot-carrier stress-induced degradation of GaN high electron mobility transistors

Lixiang Chen(陈丽香), Min Ma(马敏), Jiecheng Cao(曹杰程), Jiawei Sun(孙佳惟), Miaoling Que(阙妙玲), and Yunfei Sun(孙云飞)
Chin. Phys. B, 2021, 30 (**10**): 108502. DOI: 10.1088/1674-1056/ac1efd

A 2DEG back-gated graphene/AlGaN deep-ultraviolet photodetector with ultrahigh responsivity

Jinhui Gao(高金辉), Yehao Li(李叶豪), Yuxuan Hu(胡宇轩), Zhitong Wang(王志通), Anqi Hu(胡安琪), and Xia Guo(郭霞)\ccclink
Chin. Phys. B, 2020, 29 (**12**): 128502. DOI: 10.1088/1674-1056/abb3eb

---

RAPID COMMUNICATION

Novel double channel reverse conducting GaN HEMT with an integrated MOS-channel diode

Xintong Xie(谢欣桐), Cheng Zhang(张成), Zhijia Zhao(赵智家), Jie Wei(魏杰), Xiaorong Luo(罗小蓉)†, and Bo Zhang(张波)

School of Electronic Science and Engineering, University of Electronic Science and Technology of China, Chengdu 610054, *China*

(Received 25 February 2023; revised manuscript received 22 May 2023; accepted manuscript online 28 June 2023)

A novel normally-off double channel reverse conducting (DCRC) HEMT with an integrated MOS-channel diode (MCD) is proposed and investigated by TCAD simulation. The proposed structure has two features: one is double heterojunctions to form dual 2DEG channels named the 1st path and the 2nd path for reverse conduction, and the other is the MCD forming by the trench source metal, source dielectric, and GaN. At the initial reverse conduction stage, the MCD acts as a switch to control the 1st path which would be turned on prior to the 2nd path. Because of the introduction of the 1st path, the DCRC-HEMT has an additional reverse conducting channel to help enhance the reverse conduction performance. Compared with the conventional HEMT (Conv. HEMT), the DCRC-HEMT can obtain a low reverse turn-on voltage (V_{RT}) and its V_{RT} is independent of the gate–source bias (V_{GS}) at the same time. The DCRC-HEMT achieves the V_{RT} of 0.62 V, which is 59.7% and 75.9% lower than that of the Conv. HEMT at $V_{GS} = 0$ V and -1 V, respectively. In addition, the forward conduction capability and blocking characteristics almost remain unchanged. In the end, the key fabrication flows of DCRC-HEMT are presented.

Keywords: AlGaN/GaN, HEMT, double-channel, reverse conduction

PACS: 85.30.De, 85.30.Tv, 73.40.Qv, 51.50.+v **DOI:** 10.1088/1674-1056/ace248

1. Introduction

GaN-based power devices are promising candidates for next-generation power switching applications owing to their superior device properties, including low specific on-resistance ($R_{on,sp}$), low switching loss, and high breakdown voltage (BV).[1–4] In many power switching circuits such as DC–AC inverters and boost converters, low-loss reverse conduction of the power transistors is required to provide a free-wheeling current path so that the inductive load current would not be disrupted and high voltage peaks are suppressed.[5]

The conventional GaN HEMT itself can reversely conduct, and its reverse turn-on voltage (V_{RT}) depends on the gate–source bias (V_{GS}) and threshold voltage (V_{th}) ($V_{RT} = |V_{th} - V_{GS}|$).[6–8] In practical power switching applications, V_{RT} would even further increase since a negative V_{GS} is often employed to prevent false turn-on and increase noise immunity.[9] An externally anti-paralleled Schottky barrier diode (SBD) can obtain low reverse conduction loss[10] but introduces additional parasitic parameters[11] and increases the total cost.[12] Embedding Schottky contact is another method,[13–17] but this may sacrifice the forward conduction area[18,19] and reduce BV.[13,20,21]

In this work, we propose a novel normally-off double channel reverse conducting (DCRC) HEMT with an integrated MOS-channel diode to achieve low V_{RT}. Also, its parameters are optimized to maintain superior forward conduction capability and blocking characteristics. Finally, the feasible process steps of DCRC-HEMT are given.

2. Device structure and operation mechanism

Figure 1 shows the schematic cross-sectional view of the DCRC-HEMT and Conv. HEMT. The DCRC-HEMT is fabricated on a AlGaN/GaN/AlGaN/GaN multiple heterojunction platform, which forms double 2DEG channels named the 1st path and the 2nd path. The source metal, HfO_2 dielectric, and 1st GaN form an integrated MOS-channel diode (MCD) acting as a switch to control the 1st path, which consists of a metal–insulator–semiconductor (MIS) structure. L and t_{ox} are the length and thickness of HfO_2 in the MIS structure, respectively; N_1 of 10^{15} cm^{-3} is the doping concentration of the 1st GaN. T is the thickness of the 2nd GaN layer. The optimal values of L, t_{ox}, and T are 0.2 μm, 15 nm, and 1 μm, respectively. The other corresponding parameters of the DCRC and Conv. HEMT are kept the same. Table 1 gives the main dimensional parameters of the DCRC and Conv. HEMT. Simulations have been carried out in Sentaurus TCAD,[22] and physics models are used to accurate the simulation such as Piezoelectric_Polarization (strain) model, mobility models, e.g., DopingDependence and HighFieldSaturation, SRH recombination model, and eBarrierTunneling model. The acceptor traps (1×10^{17} cm^{-3}) are added in both the 1st and the 2nd GaN to suppress leakage current.[23] The

†Corresponding author. E-mail: xrluo@uestc.edu.cn

© 2023 Chinese Physical Society and IOP Publishing Ltd

donor traps (5×10^{13} cm^{-3}) are placed at the interface of 2nd GaN/1st AlGaN and SiN_x/2nd AlGaN to serve as the source of 2DEG in the 1st path[24] and the 2nd path,[25] respectively. The effective electron mobility in the 2DEG channel is set as 1717 cm^2/V·s,[26] and the effective electron mobility along the MCD channel is set as 165 cm^2/V·s, owing to the etch damage.[27]

Figure 2 shows the equivalent circuits and current flows of the DCRC-HEMT at different operating states. In the reverse conduction state with $V_{RT} < |V_{DS}| \le |V_{th} - V_{GS}|$ and $V_{GS} < 0$ V in Figs. 2(a) and 2(b), the MCD is turned on with the accumulation layer under the source trench. However, the 2DEG under p-GaN in the 2nd path is depleted. As $|V_{DS}|$ exceeds $|V_{th} - V_{GS}|$ in Figs. 2(c) and 2(d), the 2nd path is then turned on. Consequently, two paths participate in reverse conduction and the reverse current capacity is improved. In the on-state with $V_{GS} > V_{th}$ and $V_{DS} > 0$ V in Figs. 2(e) and 2(f), only the 2nd path turns on, while MCD is pinched off. Consequently, the forward conducting characteristics would not be influenced by the MCD.

Table 1. Main dimensional parameters.

Parameter	Value	Parameter	Value
L_{gs} (μm)	1	$t_{1st\ AlGaN}$ (nm)	15
L_g (μm)	1	$t_{1st\ GaN}$ (μm)	2
L_{FP} (μm)	5	$t_{2nd\ AlGaN}$ (nm)	15
L_{gd} (μm)	9.5	$t_{C-AlGaN}$ (nm)	15
t_{P-GaN} (nm)	110	t_{C-GaN} (μm)	2

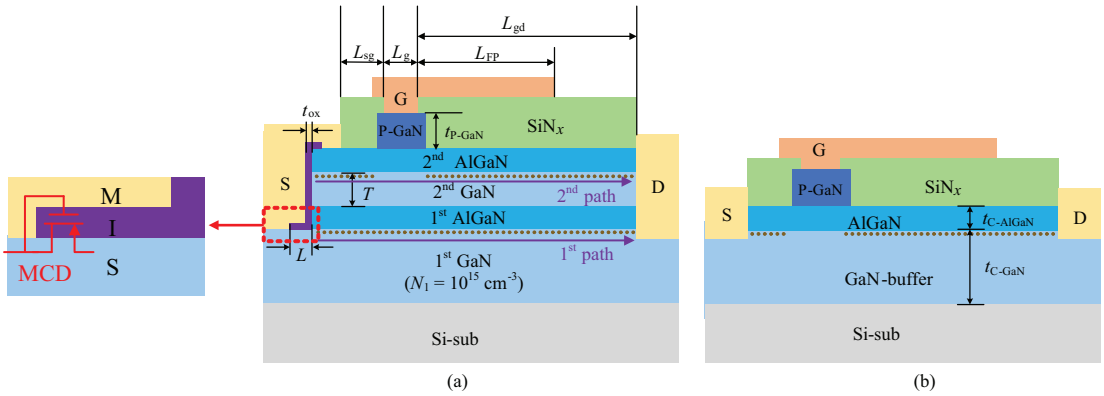


Fig. 1. Schematic cross-section of (a) DCRC-HEMT and (b) Conv. HEMT.

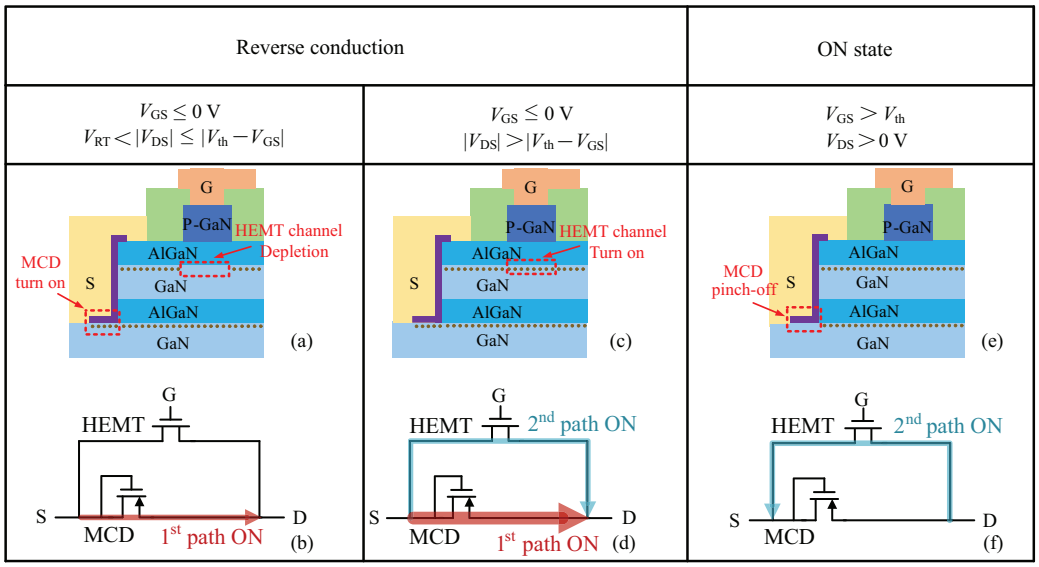


Fig. 2. Current paths and equivalent circuits of the DCRC-HEMT at different operation states.

3. Results and discussion

Figure 3(a) gives the log-scale reverse conduction characteristics to clearly illustrate V_{RT}. The V_{RT} is defined as the $|V_{DS}|$ at $|I_{DS}| = 1$ mA/mm. For DCRC-HEMT, when $V_{RT} < |V_{DS}| \le |V_{th} - V_{GS}|$, only the 1st path is turned on, as shown by point M, which is only controlled by MCD instead of V_{GS}. Therefore, the V_{RT} of DCRC-HEMT is independent of V_{GS}. When V_{GS} varies from 0 V to −1 V, the V_{RT} of the DCRC-HEMT keeps 0.62 V (i.e., at points M and M'), while the V_{RT} of Conv. HEMT shifts from 1.54 V to 2.57 V, denoted as the green arrow from O to P point in Fig. 3(a). Compared with the Conv. HEMT, the DCRC-HEMT realizes 59.7% and 75.9% reduction of the V_{RT} at $V_{GS} = 0$ V and −1 V, respec-

tively. For the curves of DCRC-HEMT, the current deviation between the solid and dashed lines at point O' suggests the turn-on of the 2nd path. The turn-on voltage of the 2nd path (i.e., at point O') is equal to that of the Conv. HEMT, i.e., at $V_{RT} = 1.54$ V at point O. Figure 3(b) shows the linear-scale reverse current through the 1st path ($|I_1|$) and 2nd path ($|I_2|$) in DCRC-HEMT at $V_{GS} = 0$ V and -1 V, which satisfies the equation $|I_1| + |I_2| = |I_{DS}|$. It can be verified that the deviation of $|I_{DS}|$ and $|I_1|$ occurs at point O' with 1.54 V or at point P' with 2.57 V, which corresponds to the turn-on voltage of the 2nd path at $V_{GS} = 0$ V or -1 V, respectively. Figures 3(c)–3(f) demonstrate the turn-on sequence of the 1st path and 2nd path and their corresponding turn-on voltages on the condition of $V_{GS} = 0$ V and -1 V.

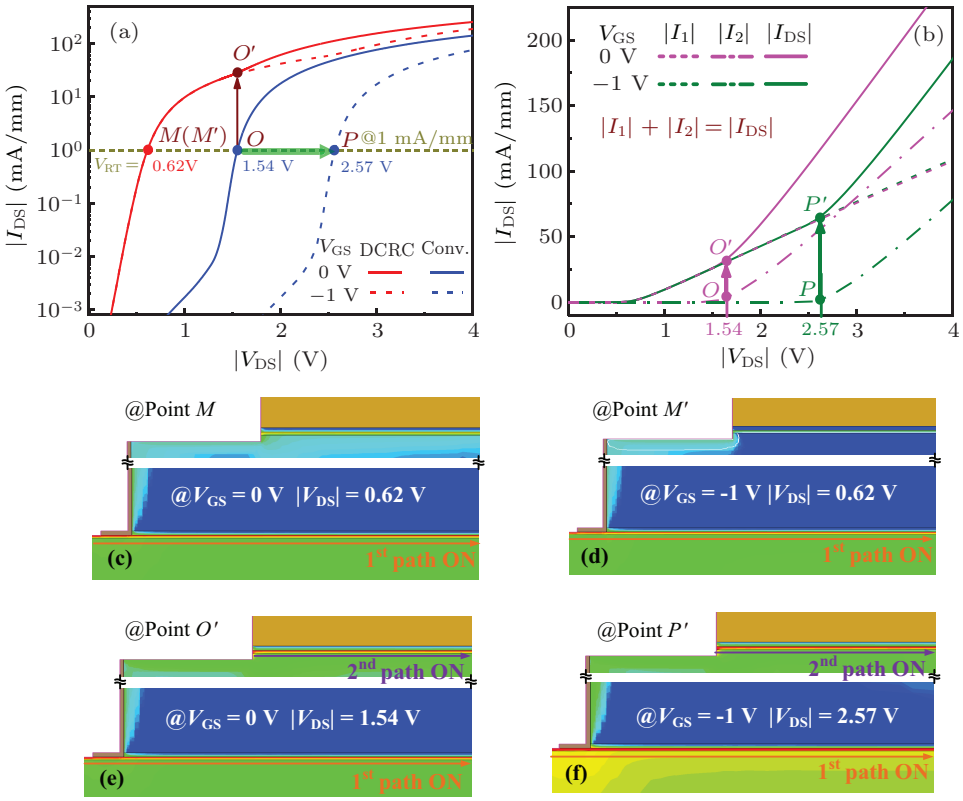


Fig. 3. Reverse conduction characteristics of the devices: (a) log-scale coordinate and (b) linear-scale coordinate. (c)–(f) Current contours for DCRC-HEMT at different conditions.

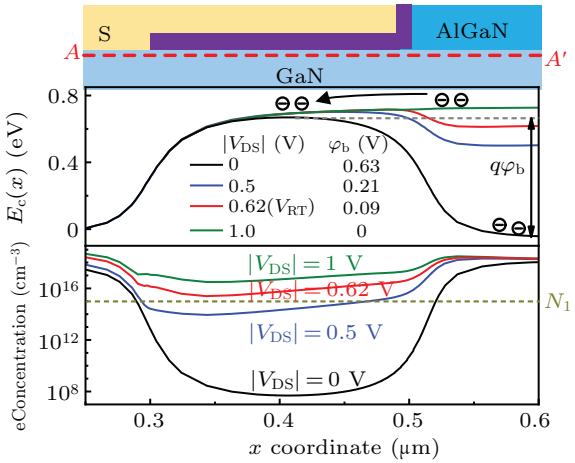


Fig. 4. Conduction band energy extracted and electron concentration distribution along cutline AA'.

Figure 4 shows the extracted conduction band energy curves ($E_c(x)$) and electron concentration distributions along the cutline AA' at different $|V_{DS}|$, respectively. When $|V_{DS}|$ increases from 0 V to 0.62 V and 1 V, the barrier height ($q\varphi_b$) steadily decreases and even disappears. The HfO_2/GaN interface under the source metal changes from depletion to accumulation state, and the electron concentration increases from lower than N_1 to higher than N_1 (although is still lower than the concentration of 2DEG). As a result, the MCD is turned on.

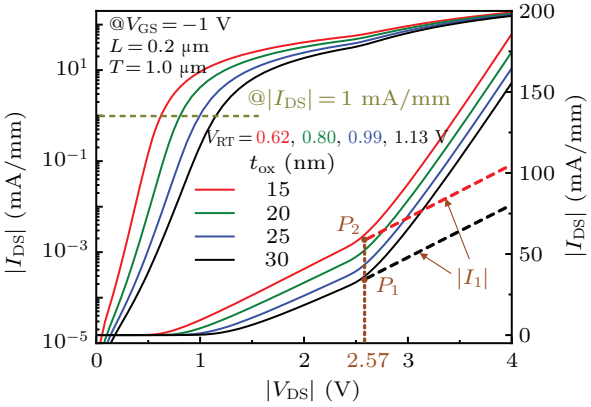


Fig. 5. Reverse conduction characteristic as a function of t_{ox}.

Figure 5 shows the log-scale and linear-scale reverse conduction characteristics of DCRC-HEMT as a function of t_{ox} at

$V_{GS} = -1$ V. The thicker t_{ox} leads to a weaker electron accumulation effect along the channel in MCD, therefore, the V_{RT} increases from 0.62 V at 15 nm to 1.13 V at 30 nm. However, the turn-on of the 2nd path is independent of t_{ox}, so points P_1 and P_2 almost keep the same value of 2.57 V as discussed in Fig. 3.

Figures 6(a) and 6(b) show the influence of L on reverse conduction characteristics and BV. It can be seen in Fig. 6(a) that V_{RT} increases slightly with the increasing L. As shown in Fig. 6(b), BV is sensitive to the variation of L when $L \leq 0.15$ μm. However, when $L \geq 0.20$ μm, the BV and V_{RT} of MCD almost keep constant. The optimized region represented in Fig. 6(b) could simultaneously fulfill the requirement of high BV and low V_{RT}. Figure 6(c) shows the $E_c(x)$ and electron concentration distributions along the cutline AA' (see Fig. 4) at different L. Owing to the short-channel effect, both the barrier height and width decrease with the decreasing L when $L < 0.15$ μm. Figures 6(d)–6(e) compare the leakage current distribution along MCD with $L = 0.1$ μm and 0.2 μm at their own BVs of 459 V and 686 V. As a result, the short-channel effect in DCRC-HEMT with $L = 0.1$ μm would lead to premature punch-through breakdown with $I_{DS} = 1$ μA/mm at the forward blocking state.

Figure 7 shows the blocking characteristics of the DCRC-HEMT with different T. High potential from drain is conducted through the 1st path of low resistance, attracting electrons from the source. The lower T means the lower distributed resistance R from the source to the 1st path. Therefore, more electrons are prone to flow through the 2nd GaN vertically to the 1st path. Thus, to suppress the high leakage current, T should not be too low.

Figure 8 gives the transfer and output characteristics of DCRC-HEMT and Conv. HEMT. Figure 8(a) shows that the DCRC and Conv. HEMT exhibit normally-off operation with $V_{th} = 1.52$ V and 1.54 V at $I_{DS} = 1$ mA/mm, respectively. Figure 8(b) indicates that the on-state performances of DCRC-HEMT almost keep consistent with that of the Conv. HEMT, which is because the 1st path does not contribute to the forward conduction.

Figure 9 shows the key fabrication of the DCRC-HEMT, which starts with forming 110-nm-thick p-GaN on a double-channel heterostructure based on the GaN-on-Si platform. The mesa isolation is fabricated by Cl_2/BCl_3-based inductively coupled plasma (ICP). Then the p-GaN gate is etched by ICP and passivation layers are formed by low pressure chemical vapor deposition (LPCVD) in Fig. 9(b). Afterwards, digital etching is used to form the source and drain trenches and mitigate the damages, including ICP etching, plasma oxidation and wet-etching in Fig. 9(c). Subsequently, dielectric deposition is carried out after the surface treatment, followed by partial etching to expose the source and drain Ohmic contact region, as shown in Fig. 9(d). In Fig. 9(e), a metal stack of Ti/Al/Ni/Au is deposited with the low-temperature Ohmic process and then is lifted-off to form the source/drain contact. Finally, the gate electrode is formed by e-beam evaporation and lift-off after selectively removing SiN_x by reactive ion etching (RIE) in Fig. 9(f).

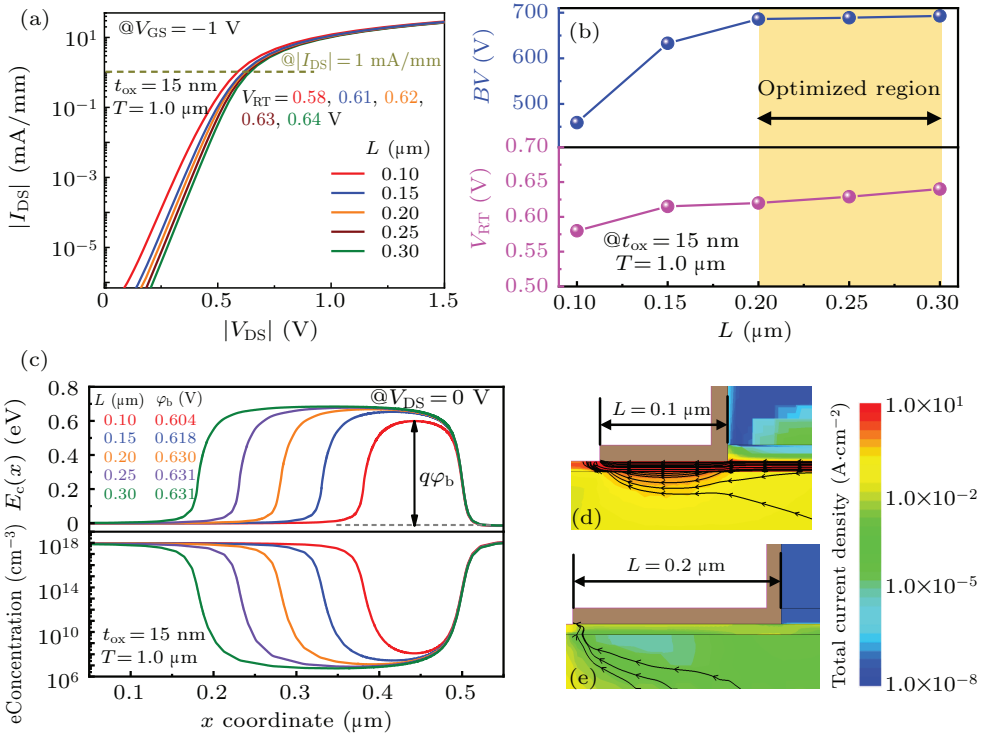


Fig. 6. (a) Reverse conduction characteristic as a function of L. (b) Influence of L on BV and V_{RT}. (c) Conduction band energy and corresponding electron density distribution along cutline AA'. Leakage current flowlines distributions of MCD with (d) $L = 0.1$ μm and (e) 0.2 μm.

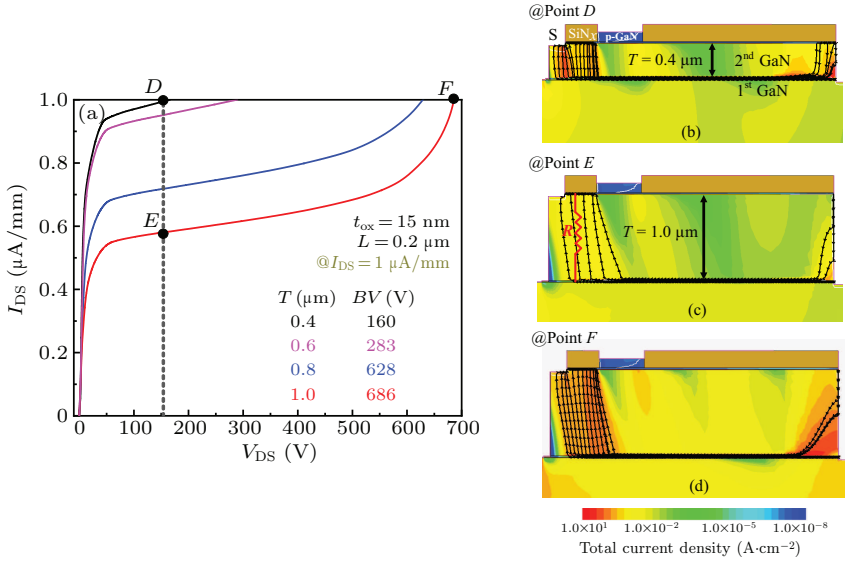


Fig. 7. (a) Forward blocking characteristics of DCRC-HEMT with different T (0.4–1.0 μm), and leakage current flowlines distributions of DCRC-HEMT at point (b) D, (c) E and (d) F.

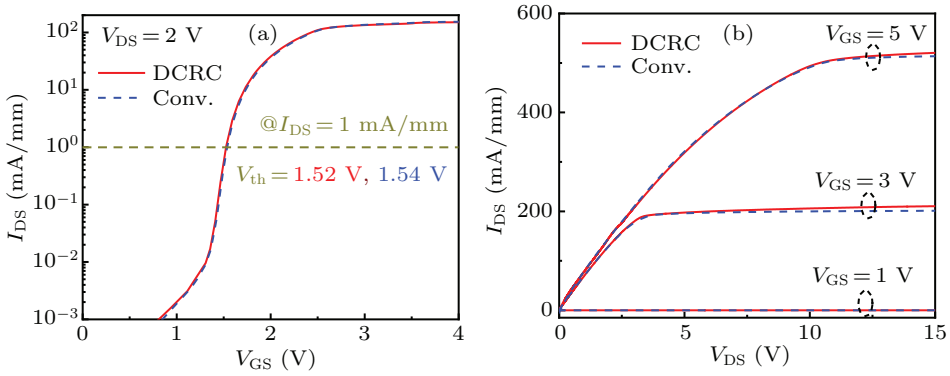


Fig. 8. (a) Transfer characteristic and (b) output characteristic of DCRC and Conv. HEMT.

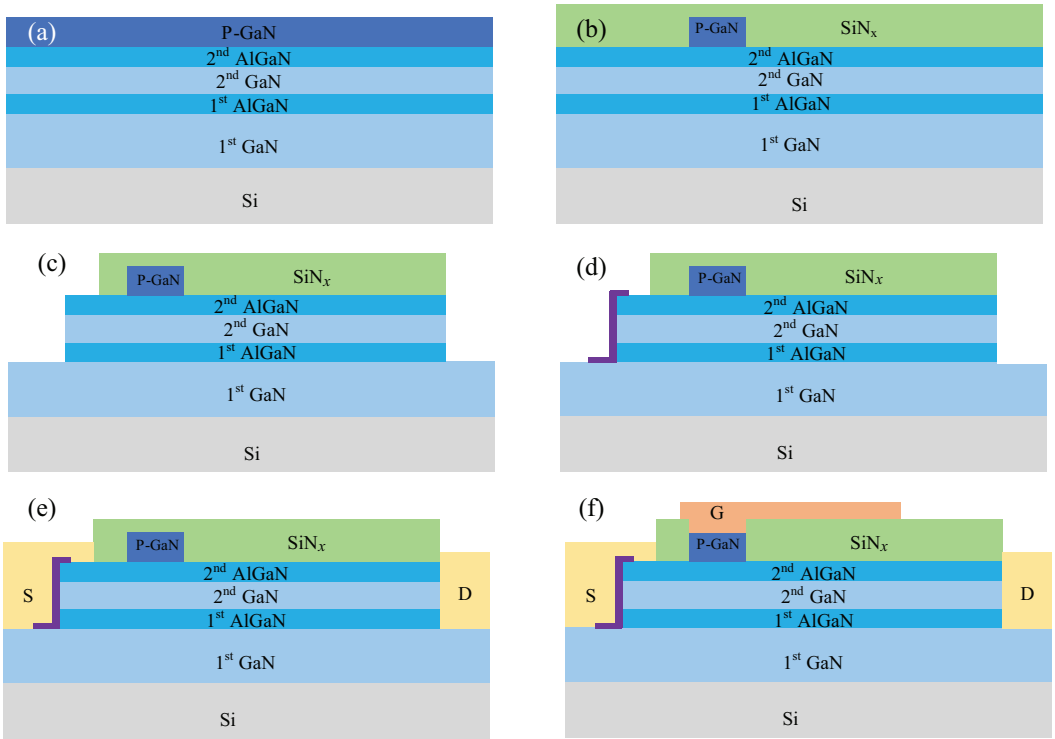


Fig. 9. Key fabrication of the DCRC-HEMT. (a) Epitaxy. (b) Gate definition and passivation layers formation. (c) Source/drain ohmic trench formation. (d) Source dielectric stack formation. (e) Source/drain electrodes. (f) Gate electrode.

4. Conclusion

In summary, a novel double-channel reverse conducting GaN HEMT with an integrated MOS-channel diode is proposed. The DCRC-HEMT provides an extra reverse current path to significantly improve the reverse current capability, maintaining the high on-state and blocking performances at the same time. The V_{RT} of 0.62 V of the DCRC-HEMT is not only low but also independent of V_{GS} and V_{th}. As a result, the proposed DCRC-HEMT has the potential to reduce reverse-conducting loss in power switching applications.

Acknowledgements

Project supported by the National Natural Science Foundations of China (Grant Nos. 61874149 and U20A20208) and the Outstanding Youth Science and Technology Foundation of China (Grant No. 2018-JCJQ-ZQ-060).

References

[1] Chen K J, Häberlen O, *et al*. 2017 *IEEE Transactions on Electron Devices* **64** 779
[2] Rupp R, Laska T, Häberlen O, *et al.* 2014 *IEEE International Electron Devices Meeting*, December 15–17, 2014, San Francisco, CA, USA, p. 2.3.1
[3] Chow T P and Tyagi R 1993 *International Symposium on Power Semiconductor Devices and ICs*, May 18–20, 1993, Monterey, CA, USA, p. 84
[4] Mishra U K, Parikh P and Wu Y F 2002 *Proc. IEEE* **90** 1022
[5] Linder S 2006 *Power semiconductors*, 1st edn. (New York: EPFL Press)
[6] Lidow A, De Rooij M, *et al.* 2019 *GaN transistors for efficient power conversion*, 3rd edn. (Chichester: John Wiley and Sons)
[7] Sørensen C, Fogsgaard M L, *et al.* 2015 *International Symposium on Power Electronics for Distributed Generation Systems*, June 22–25, 2015, Aachen, Germany, p. 1
[8] Morita T, Tamura S, *et al.* 2011 *IEEE Applied Power Electronics Conference and Exposition*, March 6–11, 2011, Fort Worth, TX, USA, p. 481
[9] Das J, Everts J, *et al*. 2011 *IEEE Electron Device Lett.* **32** 1370
[10] Reiner R, Waltereit P, *et al.* 2015 *IEEE International Symposium on Power Semiconductor Devices & ICs*, May 10–14, 2015, Hong Kong, China, p. 45
[11] Zhu R, Zhou Q, *et al.* 2018 *IEEE International Symposium on Power Semiconductor Devices and ICs*, May 13–17, 2018, Chicago, IL, USA, p. 212
[12] Kachi T, Kanechika M and Uesugi T 2011 *IEEE Compound Semiconductor Integrated Circuit Symposium*, October 16–19, 2011, Waikoloa, HI, USA, p. 1
[13] Park B R, Lee J G and Cha H Y 2013 *Appl. Phys. Expr.* **6** 031001
[14] Li S, Hou B, *et al*. 2021 *IEEE Transactions on Electron Device* **68** 931
[15] Lei J, Wei J, *et al*. 2019 *IEEE Transactions on Electron Devices* **66** 2106
[16] Yi B, Wu Z, *et al*. 2021 *IEEE Transactions on Electron Devices* **68** 6039
[17] Lei J, Wei J, *et al.* 2017 *IEEE International Electron Devices Meeting*, December 02–06, 2017, San Francisco, CA, USA, p. 25.2.1
[18] Zhang L, Wei J, *et al*. 2020 *IEEE Electron Device Lett.* **41** 341
[19] Zhang L, Wei J, *et al.* 2020 *International Symposium on Power Semiconductor Devices and ICs*, September 13–18, 2020, Vienna, Austria, p. 521
[20] Wang T, Ma J, *et al*. 2018 *IEEE Electron Device Lett.* **39** 1038
[21] Hashizume T, Kotani J and Hasegawa H. 2004 *Appl. Phys. Lett.* **84** 4884
[22] Sabui G, Parbrook P J, *et al*. 2016 *AIP Advances* **6** 055006
[23] Saito Y, Tsurumaki R, *et al*. 2017 *IEEE Transactions on Device and Materials Reliability* **18** 46
[24] Han S W, Song J, and Chu R. 2020 *IEEE Transactions on Electron Devices* **67** 69
[25] Ibbetson J P, Fini P T, *et al*. 2000 *Appl. Phys. Lett.* **77** 250
[26] Zhou Q, Chen B, *et al*. 2015 *IEEE Transactions on Electron Devices* **62** 776
[27] Liu S, Yang S, *et al*. 2014 *IEEE Electron Device Lett.* **35** 723